On the correlation between hygroscopic properties and chemical composition of cloud condensation nuclei obtained from the chemical aging of soot particles with O3 and SO2

Junteng Wu, Alessandro Faccinetto, Sébastien Batut, Mathieu Cazaunau, Edouard Pangui, Nicolas Nuns, Benjamin Hanoune, Jean-François Doussin, Pascale Desgroux, Denis Petitprez

▶ **To cite this version:**

Junteng Wu, Alessandro Faccinetto, Sébastien Batut, Mathieu Cazaunau, Edouard Pangui, et al.. On the correlation between hygroscopic properties and chemical composition of cloud condensation nuclei obtained from the chemical aging of soot particles with O3 and SO2. Science of the Total Environment, 2024, 906, pp.167745. 10.1016/j.scitotenv.2023.167745 . hal-04264852

HAL Id: hal-04264852
https://hal.science/hal-04264852v1

Submitted on 26 Nov 2023

HAL is a multi-disciplinary open access archive for the deposit and dissemination of scientific research documents, whether they are published or not. The documents may come from teaching and research institutions in France or abroad, or from public or private research centers.

L'archive ouverte pluridisciplinaire **HAL**, est destinée au dépôt et à la diffusion de documents scientifiques de niveau recherche, publiés ou non, émanant des établissements d'enseignement et de recherche français ou étrangers, des laboratoires publics ou privés.

Science of the Total Environment 906 (2024) 167745

Contents lists available at ScienceDirect

Science of the Total Environment

journal homepage: www.elsevier.com/locate/scitotenv

On the correlation between hygroscopic properties and chemical composition of cloud condensation nuclei obtained from the chemical aging of soot particles with O_3 and SO_2

Junteng Wu [a], Alessandro Faccinetto [a], Sébastien Batut [a], Mathieu Cazaunau [b], Edouard Pangui [b], Nicolas Nuns [c], Benjamin Hanoune [a], Jean-François Doussin [b], Pascale Desgroux [a], Denis Petitprez [a,*]

[a] Univ. Lille, CNRS, UMR 8522 - PC2A – Physicochimie des Processus de Combustion et de l'Atmosphère, F-59000 Lille, France
[b] Univ. Paris Est Créteil and Université Paris Cité, CNRS, LISA, F-94010 Créteil, France
[c] Univ. Lille, CNRS, INRAE, Centrale Lille, Univ. Artois, FR 2638 – IMEC – Institut Michel-Eugène Chevreul, F-59000 Lille, France

HIGHLIGHTS

- Activation of soot particles obtained from the combustion of kerosene is evaluated.
- The interplay of aging mechanisms (O_3 and SO_2) enhances soot particles activation.
- Aged soot particles show comparable activity to highly hygroscopic particle.
- Chemical composition and hygroscopic properties of aged particles are correlated.

GRAPHICAL ABSTRACT

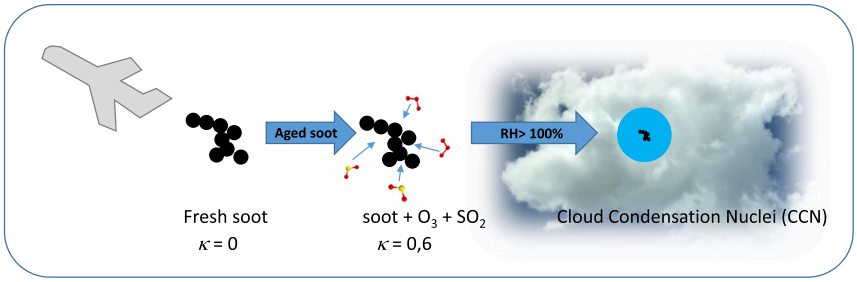

ARTICLE INFO

Editor: Hai Guo

Keywords:
Cloud condensation nuclei
Soot
Hygroscopicity
Chemical aging
Heterogeneous reaction

ABSTRACT

Soot particles released in the atmosphere have long been investigated for their ability to affect the radiative forcing. Although freshly emitted soot particles are generally considered to yield only positive contributions to the radiative forcing, atmospheric aging can activate them into efficient cloud condensation or ice nuclei, which can trigger the formation of persistent clouds and ultimately provide a negative contribution to the radiative forcing. Depending on their residence time in the atmosphere, soot particles can undergo several physical and chemical aging processes that affect their chemical composition, particle size distribution and morphology, and ultimately their optical and hygroscopic properties. The impact of the physical-chemical aging on the properties of soot particles is still difficult to quantify, as well as their effect on the radiative forcing of the atmosphere.

This work investigates the hygroscopic properties of chemically aged soot particles obtained from the combustion of aviation fuel, and in particular the interplay between aging mechanisms initiated by two widespread atmospheric oxidizers (O_3 and SO_2). Activation is measured in water supersaturation conditions using a cloud condensation nuclei counter. Once particle morphology and size distribution are taken into account, the hygroscopicity parameter κ is derived using κ-Köhler theory and correlated to the change of the chemical composition of the particles aged in a simulation chamber. While fresh soot particles are poor cloud condensation

* Corresponding author.
E-mail address: denis.petitprez@univ-lille.fr (D. Petitprez).

https://doi.org/10.1016/j.scitotenv.2023.167745
Received 21 July 2023; Received in revised form 15 September 2023; Accepted 9 October 2023
Available online 11 October 2023
0048-9697/© 2023 Elsevier B.V. All rights reserved.

nuclei ($\kappa < 10^{-4}$) and are not significantly affected by either O_3 or SO_2 at the timescale of the experiments, rapid activation is observed when they are simultaneously exposed to both oxidizers. Activated particles become efficient cloud condensation nuclei, comparable to the highly hygroscopic particulate matter typically found in the atmosphere (κ = 0.2–0.6 at RH = 20 %). Statistical analysis reveals a correlation between the activation and sulfur-containing ions detected on the chemically aged particles that are absent from the fresh particles.

1. Introduction

Soot particles formed from the incomplete combustion of hydrocarbons have a significant effect on the climate when emitted in the atmosphere as they strongly absorb shortwave radiation, which results in a positive contribution to the radiative forcing (Bellouin et al., 2020; Bond and Bergstrom, 2006). In addition, depending on their initial size distribution, soot particles can persist in the troposphere for hundreds of hours (Q. Wang et al., 2014; X. Wang et al., 2014). This period is sufficiently long for atmospheric aging processes to modify the physicochemical properties of the freshly emitted soot particles (Moteki, 2023), in particular their hygroscopicity, transforming them into cloud condensation nuclei (CCN) (He et al., 2016; Zhang et al., 2008) or ice nuclei (IN) (Mahrt et al., 2018) when transported in the upper troposphere. CCN and IN can trigger the formation of persistent clouds, resulting in a net negative contribution to the radiative forcing. The best estimation of the effective radiative forcing is currently 0.11 [−0.20 to 0.42] W m^{-2}(Szopa et al., 2021). This wide uncertainty (in magnitude and sign) is related to the physical and chemical transformations of soot particles in the atmosphere (i.e. aging, mixing) and their interactions with clouds (i.e. contrails (Kärcher, 2018), biomass burning (Mallet et al., 2020)) and the cryosphere (Hansen and Nazarenko, 2004), a set of processes that are quite difficult to quantify (Lohmann et al., 2020).

Freshly emitted soot particles are fractal-like aggregates containing up to hundreds of roughly spherical primary particles mainly composed of carbon and hydrogen, with chemical and physical properties highly dependent on the combustion conditions (D'Anna, 2009; Wang, 2011; Martin et al., 2022). Once emitted in the atmosphere, soot particles may undergo several aging processes that have been widely investigated both in the laboratory and in real atmospheric conditions such as photochemical and heterogeneous oxidation or adsorption/deposition of gas-phase species (Grimonprez et al., 2018; Gross and Bertram, 2008; Guilloteau et al., 2010; Han et al., 2012; Lambe et al., 2015; Lelievre et al., 2004; Li et al., 2017; Liu et al., 2010; Peng et al., 2017, 2016; Tritscher et al., 2011). Freshly emitted soot particles have long been known to be poor CCN (Grimonprez et al., 2018; Hagen et al., 1989; Weingartner et al., 1997; Popovicheva et al., 2008). However, atmospheric aging can significantly impact their chemical composition and therefore deeply affect their hygroscopic properties. Extensive laboratory studies under controlled laboratory conditions have demonstrated that fresh soot particles can be turned into efficient CCN by photochemical aging (Li et al., 2022, 2018), or alternatively by chemical aging with OH and NO_3 radicals or O_3 under atmospherically relevant conditions (Friebel et al., 2019; Friebel and Mensah, 2019; Grimonprez et al., 2018; Lambe et al., 2015; Tritscher et al., 2011; Wittbom et al., 2014). These results are also confirmed by field measurements showing that soot particles can undergo changes of morphology, chemical composition and optical properties during aging (Bhandari et al., 2019; Peng et al., 2017; Zhang et al., 2008).

Among these research works, some have focused on the hygroscopicity of soot particles directly emitted in the upper troposphere by aircraft engines to evaluate their role in contrails formation (Kärcher, 2018; Khou et al., 2017; Petzold et al., 2005; Schumann et al., 2017). Contrails, which can evolve into persistent clouds, give a small but positive contribution to the radiative forcing that is becoming more and more important as the volume of air traffic increases (Klöwer et al., 2021). Even if there is no clear consensus in the previously cited literature, contrails formation is often explained by rapid activation following the formation or deposition at the surface of soot particles of sulfates (SO_4^{2-}). Alternatively, exposure of soot particles to OH radicals has also been shown to significantly enhance activation (Lambe et al., 2015). Therefore, soot particles oxidized by OH radicals, which are present at high concentration in aircraft turbines, have been suggested to be an important source of CCN in aircraft exhausts (Grimonprez et al., 2021).

The reaction HO + SO_2 (+ O_2, H_2O) → H_2SO_4 + HO_2 has been long known to dominate in the gas phase under tropospheric conditions (Stockwell and Calvert, 1983). The resulting sulfates ($H_2SO_4 + 2H_2O \rightarrow HSO_4^- + H_3O^+ + H_2O \rightleftarrows SO_4^{2-} + 2H_3O^+$) can participate to heterogeneous processes (for instance, deposit onto existing aerosol particles) or, if present in sufficiently high concentration, to the homogeneous nucleation of ultrafine particles (Sipilä et al., 2010). The presence of ammonia (Kirkby et al., 2011) or oxidized biogenic organic compounds (Riccobono et al., 2014) stabilizes SO_4^{2-} and their clusters. Formation of SO_4^{2-} may also result from the reaction of SO_2 with stabilized Criegee intermediate resulting from the ozonolysis of unsaturated organics (Berndt et al., 2012). On the other hand, laboratory measurements support the idea that multiphase chemistry on the surface of solid or aqueous particles also play an important role on the conversion of SO_2 during formation of SO_4^{2-} (Cheng et al., 2016; Liu et al., 2021; Ma et al., 2023; Quan et al., 2015).

Experiments performed on carbonaceous materials in controlled laboratory conditions are, however, sparse. The heterogeneous oxidation of SO_2 has been investigated by diffuse reflectance infrared Fourier transform spectroscopy (Xu et al., 2015). The authors observed that the rate of formation of SO_4^{2-} largely increases when black carbon preventively aged with O_3 is exposed to SO_2. Oxidation of SO_2 has also been studied on the surface of soot using attenuated total internal reflection infrared spectroscopy (Zhao et al., 2017) that allows following in real time the formation of SO_4^{2-}. This result is supported by calculations of the energy profiles of the reactions pathways that show a catalytic effect of soot on the oxidation of SO_2 by O_2 (He et al., 2018; He and He, 2020). However, to the best of our knowledge, no experimental study investigated the interplay of these mechanisms that could initiate activation of soot particles.

The present work focuses on investigating the changes of the hygroscopic properties of soot particles obtained from the combustion of aviation fuel (Jet A-1 kerosene) chemically aged with two widespread atmospheric oxidizers (O_3 and SO_2). The experiments have been designed to minimize the role of the gas-phase chemistry and to focus on the heterogeneous processes occurring on the soot particles. The soot activation is measured in water supersaturation conditions using a water droplets counter and the hygroscopicity parameter κ is calculated following the approach that we recently proposed (Wu et al., 2020). To describe the size-dependent particle activation process, this approach uses the particle volume equivalent diameter d_{ve} that is calculated from the mobility diameter corrected by the morphology descriptors of the soot aggregates, which are measured with a scanning mobility particle sizer (SMPS) and transmission electron microscopy (TEM), respectively. Finally, the ex situ analysis of the chemical composition of the soot particles performed by time of flight secondary ion mass spectrometry (ToF-SIMS) reveals a correlation between the increasing κ and the presence of several sulfur-containing ions in the aged particles that are absent from the fresh particles.

2. Methods

A detailed description of the experimental protocol adopted for the soot aging experiments is reported in our previous work (Grimonprez et al., 2021; Wu et al., 2020), and only relevant changes and improvements are detailed herein. Briefly, soot particles are sampled from a reference laboratory flame and size selected (Section 2.1). The monodisperse fresh soot particles are injected into the CESAM atmospheric simulation chamber at ambient temperature and pressure where they are chemically aged with O_3 and SO_2 (Section 2.2). The activated fraction against water supersaturation, from which κ is derived, is measured on-line (Section 2.3). At the end of each experiment, samples are extracted and deposited on suitable substrates for morphological (Section 2.4) and chemical (Section 2.5) analyses.

As shown in Table 1, four series of experiments are performed under different conditions. First, κ of monodisperse fresh soot particles is measured as reference value (EXP1). Then, κ of the activated particles is measured for the fresh particles exposed first to SO_2 then O_3 (EXP2), and first to O_3 then SO_2 (EXP3). The injection order of SO_2 and O_3 is swapped in EXP2 and EXP3 in order to identify the role of soot pre-treatment by SO_2 or O_3, respectively. These two experiments are carried out at very low relative humidity (RH) in the chamber (RH < 0.2 %). To assess the role of water vapor, EXP2 is repeated at RH = 20 % (EXP4).

2.1. Soot generation and sampling

In this work, a turbulent diffusion jet flame supplied with aviation grade kerosene (Jet A-1) is used to generate soot particles with controlled size distribution, morphology and chemical composition. The diffusion flame is stabilized on the same atmospheric hybrid burner described in our previous works. Briefly, a standard Holthuis burner is modified with a central direct injection high efficiency nebulizer for liquid fuels. At the tip of the nebulizer, the kerosene flow is broken into a spray by the pressurizing N_2. The spray is then ignited by the premixed methane-air flat flame ($\phi = 0.96$) stabilized on the top of the porous plug surrounding the nebulizer. The resulting turbulent flame is 21 cm high and roughly 2 cm wide. The steps leading to soot formation in diffusion flames follow a sequence starting with the fuel oxidation at the bottom of the flame, followed by acetylene formation which is the building block of the first aromatic ring (Smooke et al., 2005). Then, polycyclic aromatic hydrocarbons (PAHs) are formed and peak around 70 mm height above the burner (HAB) in our flame. PAHs and their derivatives are well-known soot precursors (Martin et al., 2022), and therefore their consumption corresponds to the formation of soot particles whose concentration peaks around 130 mm HAB in our flame. The axial distribution of PAHs and soot in the kerosene flame is schematically represented in (Grimonprez et al., 2018) and is derived from in situ measurements of PAHs by laser induced fluorescence and of soot by laser induced incandescence (Lemaire et al., 2010, 2009). In our protocol, soot particles are sampled at 130 mm on the flame axis where the concentration of hydrocarbons in the gas phase reaches its minimum, and soot particles show the lowest CCN activity when exposed to O_3 compared to other HABs (Grimonprez et al., 2018).

The sampling system used to transfer the soot particles from the flame to CESAM consists of a diluting microprobe followed by a diffusion denuder and a differential mobility analyzer (DMA 3081, TSI). The diluting microprobe is made of two concentric quartz tubes (Irimiea et al., 2018). The outer tube ends with a thin tip with a 126 μm aperture that is radially inserted into the flame. During the sampling, the dilution nitrogen flows between the tubes, mixes at the probe tip with the aerosol sampled from the flame and is extracted through the inner tube. The inner probe tube is connected downstream to the diffusion denuder which consists of a square cross section tube containing 22 parallel 260 × 50 mm sheets of activated carbon-embedded silica paper. The adsorption efficiency of the denuder is characterized by gas chromatography on a standard mixture of gaseous hydrocarbons, and verified to be higher than 94 % for hydrocarbons containing 3–7 carbon atoms (Grimonprez et al., 2018). The main improvement with respect to our previous investigations is the DMA installed downstream the probe, which allows the pre-selection of monodisperse soot particles before injection: as explained in Section 2.3, controlling the mobility size distribution of the injected particles is critical for the determination of κ. Since the mobility diameter selection operated with the DMA drastically reduces the number concentration of the injected particles, a low dilution ratio (around 20) has to be used to reach a sufficiently high number concentration of aerosol particles in CESAM (around 10^3 cm^{-3}) in a reasonably short injection time (15–30 min).

2.2. Soot aging in the CESAM atmospheric simulation chamber

The freshly emitted soot particles are injected into the stainless steel, 4.2 m^3 CESAM atmospheric simulation chamber, that has already been extensively used to investigate the aging process of aerosols (Denjean et al., 2015; Kourtchev et al., 2015; Wang et al., 2011; Yasmeen et al., 2012). During all experiments, CESAM is first filled with synthetic air (80 % N_2 and 20 % O_2). Then, soot particles are injected followed by known concentrations of O_3/SO_2. The geometry and wall properties of the chamber guarantee the lifetime of submicron particles to be at least 15 h while the ventilation system allow for a mixing time of about 1 min.

Ozone is generated by an 802 N (BMT GmbH) generator and its concentration is monitored by a Horiba APOA-370 detector. A known initial amount of SO_2 is directly injected into the chamber using a gas tight syringe, and its concentration is monitored in real time by an Environment SA SO_2 analyzer (*E*-series). The particle size distribution is continuously measured using a scanning mobility particle sizer (SMPS) consisting of a differential mobility analyzer (DMA 3081, TSI) with X-ray neutralizer (TSI 3088), and a condensation particle counter (CPC 3776, TSI). The CPC is set to work with a flow rate of 0.2 L min^{-1} and the flow ratio between sheath flow and sample flow of the DMA is fixed to 10:1. The impactor size is 0.0457 cm, which provides a cut-off diameter of 897.7 nm. The total scanning time is set to 135 s which provides a size-resolved distribution from 19.5 nm to 881.7 nm, 107 bins in total.

Fig. 1a shows a typical evolution of the aerosol particle total number concentration N_p against time (black line), and the same data corrected for the dilution and particle coagulation (red line). Details on the corrections can be found in (Doussin et al., 2023). Fig. 1b shows the contour plot of the aerosol size distribution. Two modes can be identified: the first one at ~150 nm corresponds to the mobility diameter d_m of the particles selected by the DMA, while the second mode at ~250 nm is attributed to larger and double-charged particles. No new particle formation events are detected after injection of SO_2 and O_3. This is an important observation confirming that the concentration of SO_4^{2-} in the gas phase is too low to sustain homogeneous nucleation. The absence of new particle formation is systematically verified for all experiments, and supports the current choice of the experimental conditions as suitable to

Table 1
Overview of the sampling conditions. $[O_3]_0$, $[SO_2]_0$ and $[OH]_0$ and RH_0 are the initial concentration in the simulation chamber of O_3, SO_2, and relative humidity, respectively, before injection of the soot particles (d_m = 150 nm). t_{exp} is the exposure time of soot to both O_3 and SO_2.

	$[O_3]_0$/ppm	$[SO_2]_0$/ppb	RH_0%	t_{exp}/min	κ	ToF-SIMS
EXP1	0	0	<0.2	14	$<10^{-4}$	S1
EXP2[a]	1.10	110	<0.2	14	0.07(3)	
				32	0.13(5)	S2
EXP3[b]	0.50	100	<0.2	15	0.18(7)	S3
EXP4[a]	1.10	109	20	29	0.20(7)	
				45	0.32(9)	
				68	0.5(2)	
				94	0.6(3)	S4

[a] SO_2 was injected before O_3.
[b] O_3 was injected before SO_2.

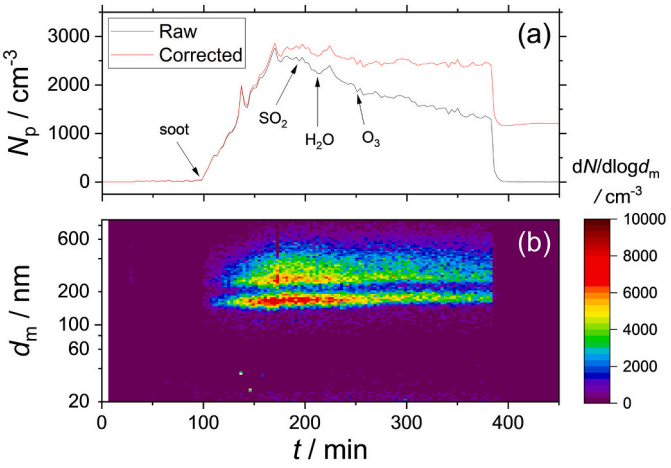

Fig. 1. (a) Total particle concentration Np against time measured by the SMPS during EXP4 (black line) and corrected by the dilution and particle wall loss effects (red line). The arrows show the injection time of SO_2, H_2O and O_3. (b) PSD against time.

minimize the injection in the chamber of reactive hydrocarbons, and thus to minimize the reactivity in the gas phase as discussed above. Further confirmation derives from one experiment (not shown here) carried out using the same aging conditions except sampling at 70 mm HAB where gaseous hydrocarbons are detected at high concentration. In this case, new particle formation events are observed immediately after the introduction of SO_2 following O_3 i.e., secondary aerosols are likely generated as a result of the gas phase chemistry as discussed above.

2.3. CCN activity and determination of the hygroscopicity parameter κ

The CCN activation behavior of fresh and aged soot particles is recorded using a cloud condensation nuclei counter (CCNc-100, Droplet Measurement Technology) and a CPC (3776, TSI) in parallel. Briefly, soot particles sampled from the chamber are equally split between the CCNc and the CPC. The number concentration of droplets ($N_{droplet}$ in cm^{-3}) formed from the monodisperse particles at a given supersaturation (*SS* in %) is measured by the CCNc. In parallel, the number concentration of monodisperse particles ($N_{particle}$ in cm^{-3}) is measured by the CPC. The activated fraction F_a is calculated as $F_a = N_{droplet} / N_{particle}$ and varies from 0 (no droplets detected) to 1 (all soot particles converted to droplets). Series of *SS*-resolved activation spectra (F_a-*SS*) are recorded by varying *SS* from 0.1 to 1.6 % in the CCNc.

According to κ-Köhler theory (Petters and Kreidenweis, 2007), at thermodynamic equilibrium the *SS* required to activate the aerosol particles and form water droplets can be described using a single hygroscopicity parameter κ. Previous studies modeled F_a-*SS* by introducing in the classical theory framework the effects of the particle size distribution (Zhao et al., 2015), of non-homogeneous aerosol chemical composition represented by a distribution of κ values (Su et al., 2010; Wu et al., 2020; Zhao et al., 2015) and of the particle morphology (Wu et al., 2020; Yon et al., 2015) that are all taken into account to retrieve κ as shown in Eq. (1).

$$F_a(SS) = \sum_{\kappa=0}^{\infty}\left\{\frac{1}{2} - \frac{1}{2}erf\left[\frac{lnd_{ve}(\kappa, SS) - ln\mu_{ve,geo}}{\sqrt{2}\,ln\sigma_{ve,geo}}\right]\right\}p(\kappa)\Delta\kappa \quad (1)$$

where $\mu_{ve,geo}$ and $\sigma_{ve,geo}$ are the mode and the geometric standard deviation of the volume equivalent diameter d_{ve}. In Eq. (1), p_κ is the probability density function of κ defined as:

$$p(\kappa) = \frac{1}{\kappa ln\sigma_{\kappa,geo}\sqrt{2\pi}} e^{-\frac{\left[ln\kappa - ln\mu_{\kappa,geo}\right]^2}{2ln^2\sigma_{\kappa,geo}}} \quad (2)$$

where $\mu_{\kappa,geo}$ and $\sigma_{\kappa,geo}$ are the geometric mean and standard deviation of κ, respectively. To calculate κ, Eqs. (1) and (2) are applied to fit each experimental F_a-*SS*. According to the model sensitivity study (Wu et al., 2020), $\sigma_{\kappa,geo}$ is fixed to 1.4 and $\mu_{\kappa,geo}$ is treated as a free parameter.

2.4. Soot morphology

At the end of each aging experiment, soot samples are collected on copper TEM microscopy grids (Holey Carbon Filter 200 Mesh) during 20 min with a flow rate of 15 L min^{-1} at 1000 mbar. The collected samples are analyzed on the FEI Tecnai G2 20 microscope (200 kV acceleration, 29,000 magnification) available at the electron microscopy facility of the University of Lille. The quantified morphological parameters are the primary particle diameter (d_{pp}) and the maximum length of the aggregate projection (L_{2D}). These parameters are used for determining the fractal dimension D_f, required to estimate d_{ve} used in Eq. (1). The measured values ($d_{pp} = 16.7$ nm and $D_f = 1.66$ for EXP1 and $d_{pp} = 17.9$ nm and $D_f = 1.68$ for EXP4) show that the morphology of the soot aggregates is only slightly affected by the aging in the chamber.

2.5. Soot chemical composition

The samples for the ToF-SIMS analyses are obtained at the end of each experiment. A detailed description of the preparation protocol is provided elsewhere (Irimiea et al., 2019, 2018). Briefly, the samples are obtained by impacting the aerosol particles extracted from the CESAM chamber onto Ti wafers. 30 min of pumping at $p = 1000$ mbar result in a clearly visible impaction site of the soot particles on the wafer surface, while condensable gas is free to diffuse and deposit all over the wafer surface. The samples are analyzed with the IONTOF TOF.SIMS5 instrument available at the surface analysis pole of the University of Lille. The loaded wafers are transferred from the preparation to the analysis chamber of the mass spectrometer (residual pressure 10^{-7} mbar) where they are irradiated with a primary ion beam of Bi_3^+ clusters (25 keV, 0.3 pA). The instrument is operated in static mode (estimated ion dose 10^{11} ions cm^{-2}). The ejected secondary ions are identified through a time-of-flight analyzer that can reach mass resolution up to 10^4. To discriminate the chemical composition of aerosol particles and condensable gas, scans in positive and negative polarity are performed in 500 × 500 μm^2 regions of interest (ROIs) on the impaction site (impaction ROIs) and on the surrounding region (halo ROIs) following the analysis protocol already established for laminar diffusion flames (Faccinetto et al., 2020). To ensure reproducibility, at least three different impaction and halo ROIs are analyzed on each sample. The identification of unknown peaks is based on the mass defect analysis of the ensemble of peaks having signal-to-noise ratio SNR > 3. All identified peaks from the deposition substrate (Ti oxides) are discarded, and the remaining peaks normalized by their partial ion count. Because of the large number of detected peaks (547 in negative polarity and 862 in positive polarity), principal component analysis (PCA) is used to reduce the dimensionality of the database and assist the data interpretation (covariance matrix, ROIs as observation and peaks as variables).

3. Results

3.1. Activation of soot by O_3 and SO_2

EXP1 is the blank experiment. The hygroscopic properties (F_a-*SS* spectra), size (SMPS), morphology (TEM) and chemical composition (ToF-SIMS) of fresh monodisperse soot particles are used as reference for all the other experiments. To verify the absence of activation, F_a is measured in real time at fixed supersaturation. $SS = 1.6$ % is chosen for being the highest *SS* that the CCNc can reliably keep over time, and thus offers the lowest detection limit for a stable measurement. In these conditions, no soot particles are activated ($F_a = 0$) over 1 h of continuous

measurements. This result confirms several previous observations showing that freshly emitted soot particles are poor CCN (Grimonprez et al., 2018; Hagen et al., 1989; Popovicheva et al., 2008; Weingartner et al., 1997).

In EXP2 (Fig. 2a, top panel), fresh monodisperse soot particles are injected followed by SO_2 and ~ 25 min later by O_3. In EXP3 (Fig. 2b, top panel) the roles of SO_2 and O_3 are inverted: fresh monodisperse soot particles are injected followed by O_3 and ~ 35 min later by SO_2. EXP2 and EXP3 are conducted under dry conditions (RH < 0.2 %). The lower panels of Fig. 2 show the corresponding F_a measured at $SS = 1.6$ %. As clearly shown in the figures, no fresh soot particles are activated ($F_a = 0$) in the presence of SO_2 (up to 100 ppb) or O_3 (up to 1 ppm) alone. This result is consistent with previous investigations showing that O_3 and SO_2 cannot independently activate soot at the timescale of these experiments (Friebel et al., 2019; Wittbom et al., 2014). However, once SO_2 and O_3 are both injected, the activated fraction quickly reaches $F_a = 1$ indicating that the totality of the soot particles is activated and forms water droplets.

Since activation consistently begins in the presence of both reactants, the exposure time t_{exp} passed after the injection of the second reactant (O_3 in EXP2 and SO_2 in EXP3) is used as reference to compare different F_a-SS measurements. Fig. 3a shows the F_a-SS spectra of the activated soot particles at different t_{exp}. F_a of EXP2 shifts to the left when increasing t_{exp} of O_3 and SO_2, i.e. the longer their permanence time in the chamber, the more efficient as CCN the aged soot particles become. Soot particles exposed first to O_3 and then to SO_2 in EXP3 are found to be more efficient CCN compared to EXP2, even at lower t_{exp}, i.e. soot particles pretreated with O_3 can be activated more easily when exposed to SO_2. This finding is in good agreement with the reported uptake of SO_2 by soot aged with O_3 being more important than by fresh soot (Xu et al., 2015). Fig. 3b shows the probability density of κ of the activated soot particles. The mean values of κ calculated for EXP2 and EXP3 are listed in Table 1. Compared to the very low value of κ of fresh soot ($\kappa < 10^{-4}$), κ of aged soot ranges from 0.07 ± 0.03 up to 0.18 ± 0.07. This result clearly shows that hydrophobic fresh soot can be efficiently transformed in CCN when exposed to O_3 and SO_2 simultaneously.

Finally, experiment EXP4 is performed in the same conditions of EXP2 except for the higher RH. After injecting the fresh soot, water vapor is injected to reach RH = 20 %. Fig. 4 shows the comparison of κ of aged soot particles exposed to SO_2 and O_3 with RH < 0.2 % (EXP2) and RH = 20 % (EXP4) conditions. At the same t_{exp}, κ of aged soot at RH = 20 % is about two times larger than at RH < 0.2 %.

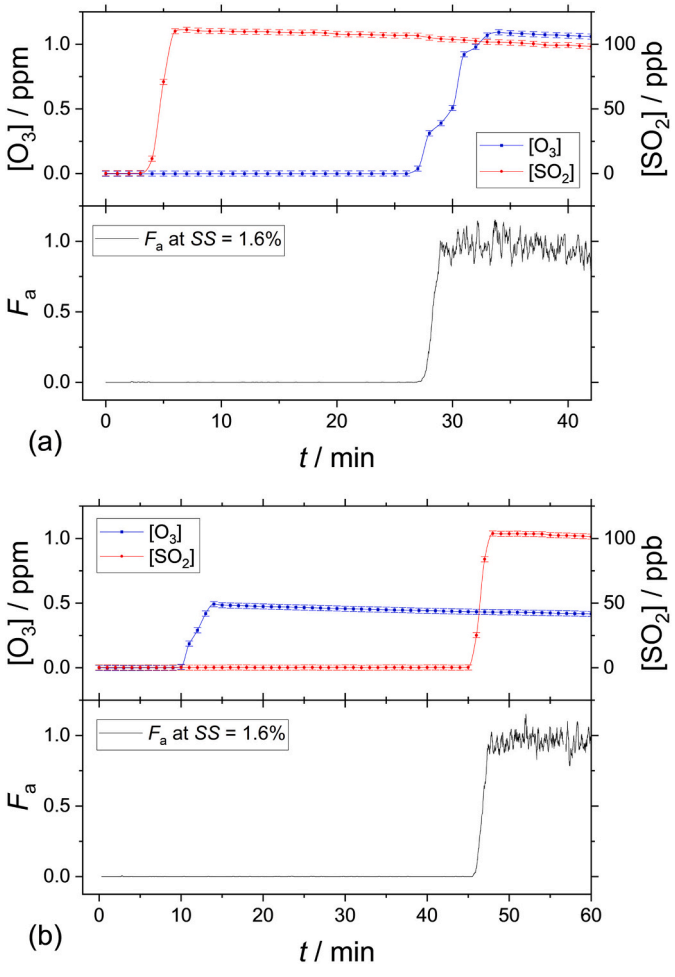

Fig. 2. Role of O_3 and SO_2 on the CCN activation of soot particles. The top panels show the concentration of O_3 and SO_2, while the bottom panels show the activated fraction F_a at fixed $SS = 1.6$ %, all monitored in real time. (a) EXP2, SO_2 is injected ~25 min before O_3. (b) EXP3, O_3 is injected ~35 min before SO_2.

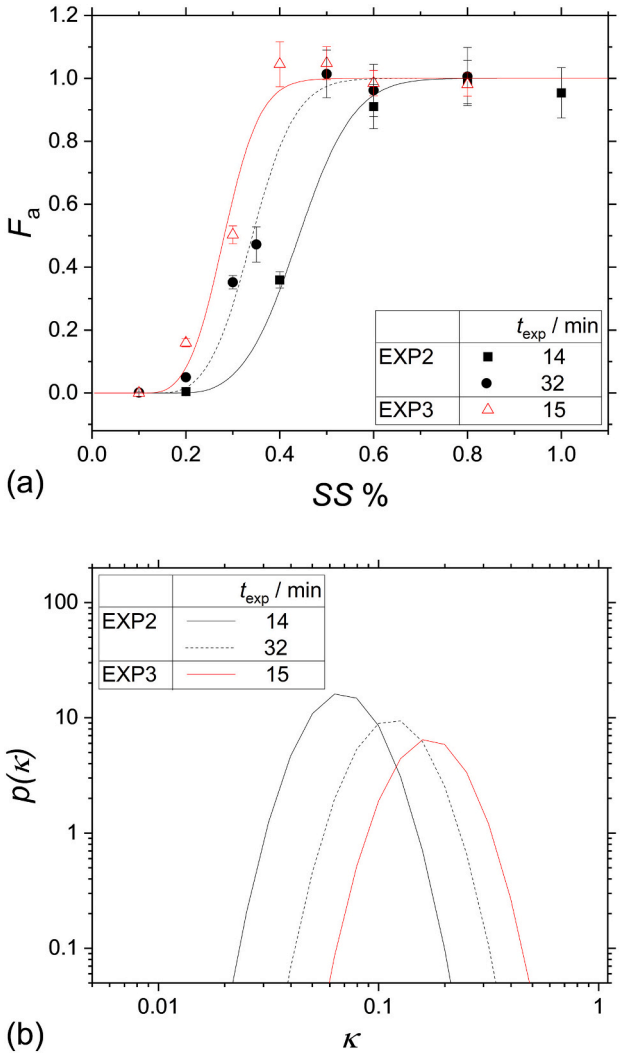

Fig. 3. Hygroscopic properties of soot activated by O_3 and SO_2 in dry condition (EXP2, RH < 0.2 %), see Table 1 for the concentrations. t_{exp} is the exposure time to both oxidizers, measured from the injection of the second oxidizer. (a) Activated fraction F_a versus SS. (b) Probability density function $p(\kappa)$ versus κ. Datapoints and lines represent experimental data and fitting curves (Eqs. (1) and (2)), respectively, from EXP2 (black) and EXP3 (red). The error bars represent the standard deviation calculated from 1 min of continuous acquisition.

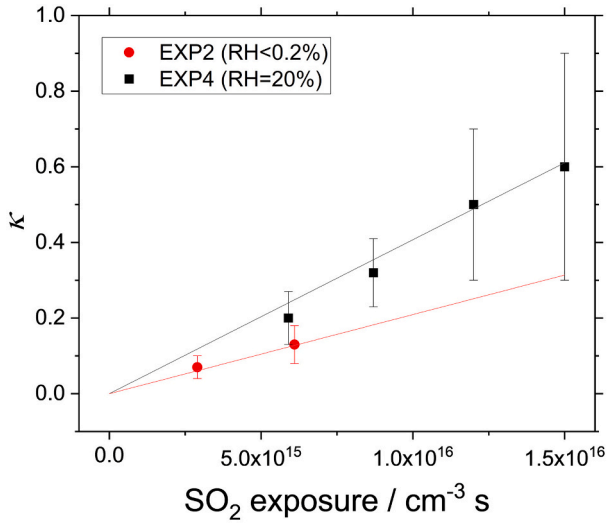

Fig. 4. κ of aged soot exposed to SO_2 and O_3 versus SO_2 exposure in dry (RH < 0.2 %, EXP2) and wet (RH = 20 %, EXP4) conditions. The lines are linear fittings. The error bars represent the FWHM of the corresponding $p(\kappa)$.

3.2. Analysis of the chemical composition of soot particles

Samples of fresh and aged soot particles are collected and analyzed by ToF-SIMS. The sampling conditions are indicated in Table 1: sample S1 contains the fresh soot particles analyzed as the blank, while samples S2, S3 and S4 contain the soot particles chemically aged with O_3 and SO_2. The analysis of the positive polarity mass spectra does not lead to useful results since the PCA cannot correlate the information extracted from the mass spectra to any other measured property. Therefore, the discussion below is limited to the analysis and interpretation of the negative polarity mass spectra.

The mass defect plot obtained from the mass spectra in negative polarity of soot particles chemically aged with O_3 and SO_2 is shown in Fig. 5. The mass spectra are rich of low-mass $C_mH_n^-$ and $C_mH_nO_p^-$ (fragment) ions likely resulting from the degradation of the carbon matrix under irradiation (high mass defect series). Larger molecular ions

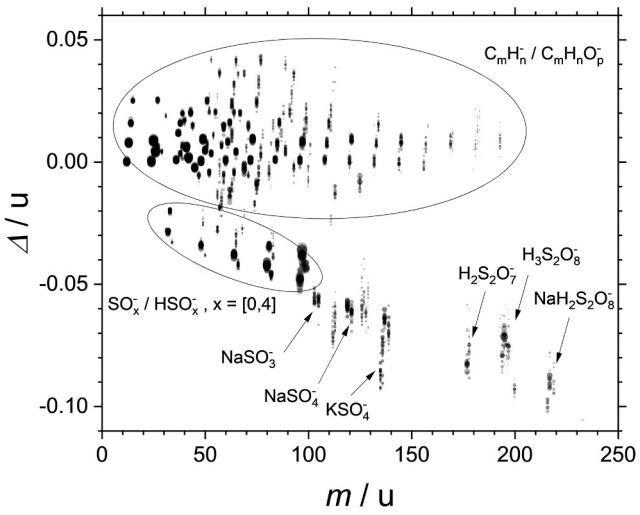

Fig. 5. Mass defect plot showing the peaks used as input for the PCA (background removed, only peaks with SNR > 3 are shown). The size of the datapoints is proportional to the logarithm of the (normalized) peak intensity. The low mass defect series mostly contains SO_3^{2-}, SO_4^{2-}, and $S_2O_8^{4-}$ along with their fragment ions partially recombined with H^+, Na^+ and K^+. The high mass defect series is typical of soot and contains $C_mH_n^-$ and $C_mH_nO_p^-$ fragment ions.

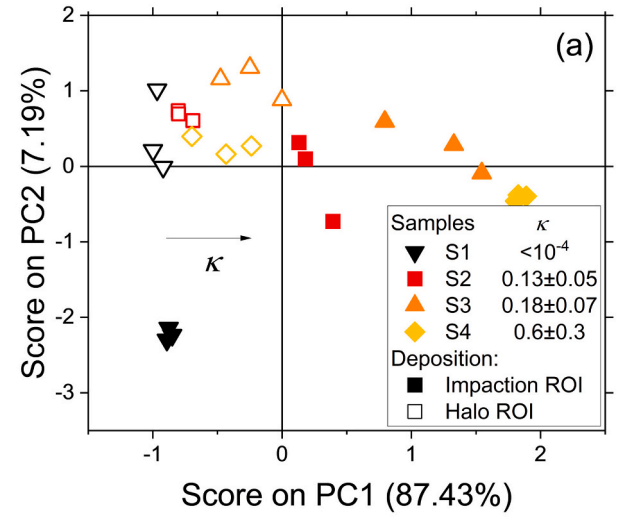

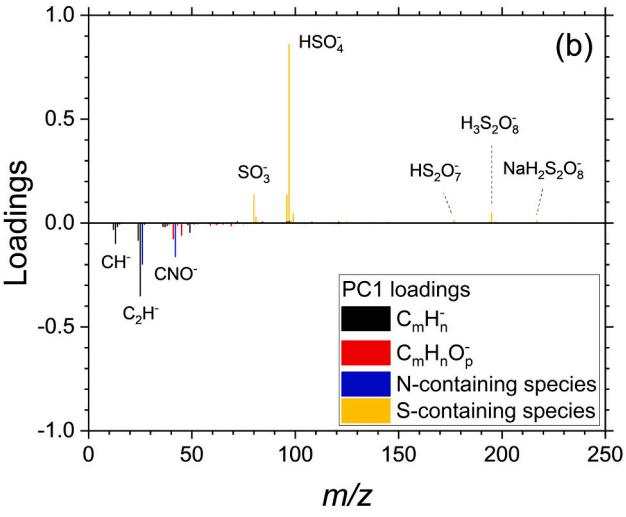

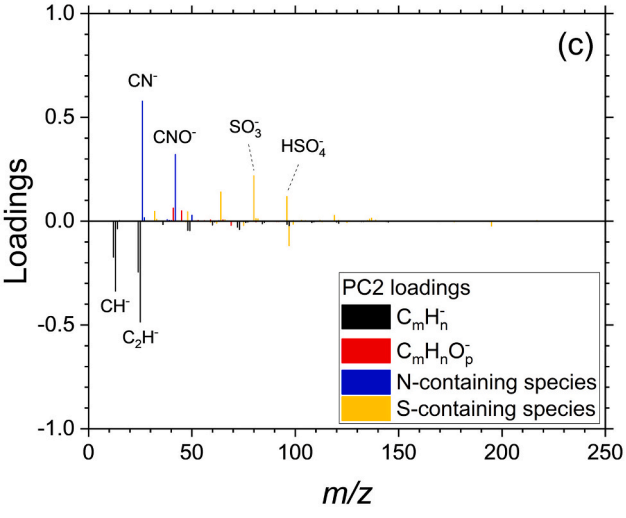

Fig. 6. Results of the PCA performed on the ToF-SIMS negative polarity mass spectra representing the chemical composition of the aged soot particles. 24 ROIs (observations) against 170 peaks (variables), covariance matrix. (a) PC2 vs. PC1 score plot. The different shapes and colors of the datapoints represent different samples as detailed in Table 1. Solid and open symbols indicate the impaction and halo ROI, respectively. (b) and (c) PC1 and PC2 loading plots, respectively.

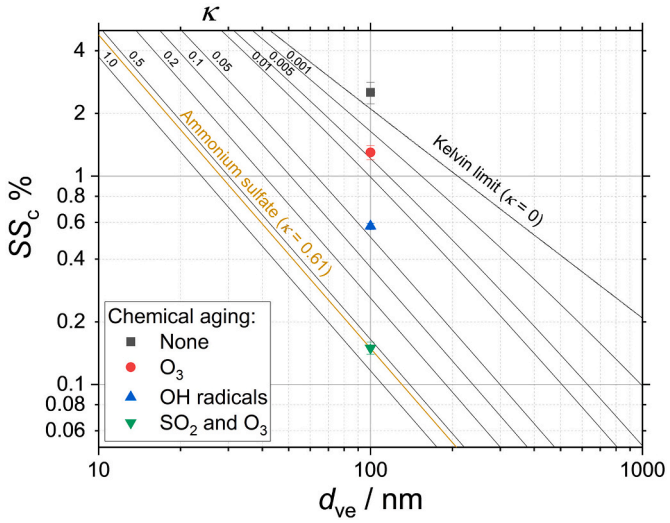

Fig. 7. Comparison of κ of CCN obtained from fresh and aged soot represented in a classical SS_c against d_{ve} diagram. The values of κ are listed in Table 2.

like polycyclic aromatic hydrocarbons typically found adsorbed on soot particles (Irimiea et al., 2019) are absent as they preferentially generate cations. Several sulfur-containing anions are identified that include: S^-, SO^-, SO_2^-, SO_3^-, HSO_3^-, SO_4^-, HSO_4^-, $NaSO_3^-$, $S_2O_3^-$, $NaSO_4^-$, $Na_2SO_3^-$, KSO_4^-, $HS_2O_7^-$, $H_2S_2O_7^-$, $H_2S_2O_8^-$, $H_3S_2O_8^-$, $NaHS_2O_7^-$, $NaHS_2O_8^-$, $NaH_2S_2O_8^-$ and $KH_2S_2O_8^-$. The most recurring anions appear to be SO_3^{2-}, SO_4^{2-} and $S_2O_8^{4-}$ partially recombined with H^+, Na^+ and K^+.

Fig. 6 shows the results of the PCA on all the available mass spectra. The analysis of the score plot (Fig. 6a) and of the loading plots of the PC1 and PC2 (Fig. 6b and c, respectively) conveys different levels of chemical information. First, in the loading plot of the PC1 only sulfur-containing ions have high positive loadings. Therefore, the transition from negative to positive scores on PC1 represents the change in the chemical composition due to the incorporation in the samples of sulfur-containing species. Second, in the score plot in Fig. 6a, all halo ROIs (S1, S2, S3 and S4) and the impaction ROIs of the fresh soot sample (S1) have negative scores in PC1, while the impaction ROIs of the samples chemically aged with O_3 and SO_2 (S2, S3 and S4) have positive scores on PC1. Raman spectroscopy analyses systematically performed on samples extracted from laboratory flames using the same impaction conditions show that soot particles are collected only on the impaction ROIs and are absent from the halo ROIs (Faccinetto et al., 2020). Therefore, the low negative scores on PC1 of the halo ROIs, comparable to those of fresh soot, clearly show that the sulfur-containing ions are found in the chemically aged particles only. Third, as shown in the score plot in Fig. 6a, κ progressively increases for increasing positive scores in PC1. In conclusions, these observations strongly suggest that the change in the hygroscopic properties of the aged soot particles is related to the sulfur-containing anions listed above that are found on the chemically aged soot particles.

The majority of the impaction and halo ROIs have low scores in PC2, with the only exception being the impaction ROIs of the blank S1. As shown in Fig. 6c, small carbon fragment ions have the highest negative loadings on PC2 in Fig. 6c. PC2 possibly represents the destruction of the particles carbon matrix regardless of the oxidation source. However, since PC2 only represents 7.19 % of the total variance, this effect is considered to be negligible when compared to the contribution of sulfur-containing ions to PC1.

4. Discussion

In this work, the hygroscopic properties of soot particles sampled from a kerosene flame and then aged with O_3 and SO_2 are studied in water supersaturation conditions using a cloud condensation nuclei counter. While freshly emitted soot particles are highly hydrophobic, they are efficiently transformed into CCN when simultaneously exposed to O_3 and SO_2. Experiments performed under dry (RH < 0.2 %) and wet (RH = 20 %) conditions show that the chemical aging is further accelerated in presence of water vapor. The hygroscopicity parameter κ is calculated at different steps of the aging for each of the experiments. For freshly emitted soot particles $\kappa < 10^{-4}$, while for chemically aged soot particles $\kappa = 0.07$–0.18 at RH < 0.2 %. At RH = 20 %, $\kappa = 0.2$–0.6 that is comparable to ammonium sulfate ($\kappa = 0.61$) (Petters and Kreidenweis, 2007) i.e. to one of the most hygroscopic chemicals found in the particulate matter in the atmosphere.

By measuring κ of soot during exposure to O_3 and SO_2, this study provides a new indicator of the chemical changes of soot particles as confirmed by the identification of the reaction products. To this means, mass spectrometry analysis shows that sulfur-containing ions are detected only on aged soot. In addition, principal component analysis highlights the existence of a correlation between the presence of sulfur-containing ions and the change of the hygroscopic behavior of aged soot. Therefore, the available evidence suggests heterogeneous reactions involving both O_3 and SO_2 on the soot particles.

The uptake of O_3 or SO_2 by carbonaceous surfaces and associated heterogeneous reactions has been the subject of numerous studies during the last decades using flow tube reactors, Knudsen cells or simulation chambers (Liu et al., 2022). Soot is oxidized by O_3 only at high exposure, and the resulting CCN typically show limited activity (Friebel et al., 2019; Friebel and Mensah, 2019; Grimonprez et al., 2018). This behavior is observed during the first period in EXP2, where soot is exposed to O_3 alone for 35 min, too short a duration to generate CCN even at the extreme $SS = 1.6$ %.

Heterogeneous reactions between *n*-hexane soot and SO_2 have been studied using attenuated total internal reflection infrared (ATR-IR) spectroscopy and ion chromatography for on-line measurement of SO_3^{2-}/SO_4^{2-} formation in a flow tube reactor (He et al., 2018; Zhao et al., 2017). Experiments carried out as a function of RH (6–70 %) show that water vapor promotes SO_2 adsorption and SO_4^{2-} formation. In addition to the role of water, the role of molecular oxygen has also been demonstrated in the oxidation process of SO_2 into SO_4^{2-} at the surface of propane soot by electron spectroscopy (Novakov et al., 1974) or on *n*-hexane soot by electron paramagnetic resonance (Chughtai et al., 1998). To explain these experimental results, the energy profiles of the reactions pathways have been calculated, and a catalytic mechanism for the oxidation of SO_2 at the surface of soot involving molecular oxygen and leading to the formation of SO_4^{2-} has been recently proposed (He

Table 2
κ of kerosene soot CCN ($d_{ve} = 100$ nm) exposed to atmospheric oxidizers. The atmospheric age represents the time needed for soot to experience in the troposphere the equivalent exposure used in the simulation chamber. The range of the atmospheric age is calculated with the range of typical concentration of each oxidizer in the troposphere: $[O_3] = 40$–55 ppb (Parrish et al., 2021), [OH] = 0.08–0.3 ppt (Mao et al., 2009; Stone et al., 2012), $[SO_2] = 2$–150 ppb (Boichu et al., 2019).

Oxidizer	κ	cm^{-3} s	Atmospheric age/h
/	$<10^{-4}$ (Grimonprez et al., 2018)	/	/
O_3	5×10^{-3} (Grimonprez et al., 2018)	2.0×10^{17}	41–56
OH	5×10^{-2} (Grimonprez et al., 2021)	1.9×10^{11}	7–26
O_3/SO_2[a]	6×10^{-1} (this work)	1.6×10^{16}	3–90

[a] Exposure calculated with respect to SO_2.

and He, 2020).

In this work, in EXP1, soot is exposed to SO_2 only for 23 min at RH < 0.2 %. Similarly to EXP2, no droplets are measured even at high supersaturation (SS = 1.6 %). We must here underline important differences concerning our experimental conditions compared to those cited above on *n*-hexane soot. First, the SO_2 concentration used in this work are in the range of 100 ppb, i.e. 1–4 orders of magnitude smaller than those used in the works cited above. Second, soot is exposed to SO_2 in a simulation chamber and not while deposited on substrates. Finally, no activation could be observed before the injection of O_3, i.e. activation of soot due to the interplay of SO_2 and O_2 (the latter available from the synthetic air used to fill the simulation chamber) can be ruled out. However, as soon as soot particles are simultaneously exposed to SO_2 and O_3, they become efficient CCN, certainly due to the formation of SO_4^{2-} on the particles as shown by ToF-SIMS analyses.

Very few works report measurements that could lead to the writing of a kinetic mechanism describing the heterogeneous conversion of SO_2 into SO_4^{2-} in the presence of ozone. For instance, a mechanism has been proposed for calcium carbonate (Li et al., 2006):

$$(SO_2)_g \leftrightarrows (SO_2)_{ads}$$

$$(SO_2)_{ads} + (H_2O)_{ads} \rightarrow (SO_3^{2-})_{ads} + 2(H^+)_{ads}$$

$$(SO_3^{2-})_{ads} + O_3 \rightarrow (SO_4^{2-})_{ads} + O_2$$

Notice that this mechanism requires water adsorbed on the $CaCO_3$ surface. In addition, the heterogeneous conversion of SO_2 into SO_4^{2-} has been extensively studied using a gas-flow sample cell coupled to a micro-FTIR spectrometer to monitor the formation of SO_4^{2-} on the surface of synthetic soot exposed to an O_3/SO_2 mixture (He et al., 2017). The mechanism specifically proposed for carbonaceous surfaces by the authors begins with the reaction of O_3 with a soot surface site (for instance, a C=C bond with neighboring CH) to form a Criegee intermediate. Then, SO_2 can react with the Criegee intermediate to form SO_4^{2-} according to:

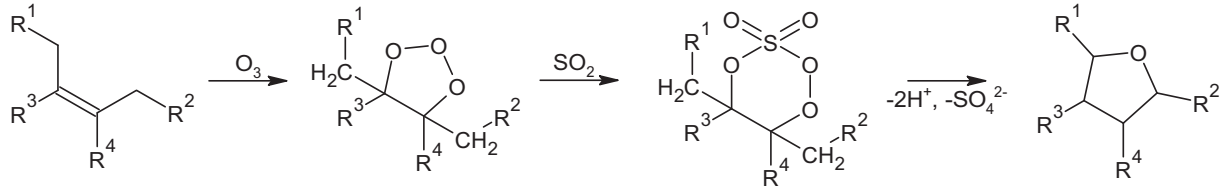

The development of a detailed kinetic model is beyond the scope of this work. However, we believe this second mechanism to be more suitable for soot particles because of the availability of hydrogen at the soot surface: in this second case, adsorbed water is not necessary like in the case of $CaCO_3$, and this fits well with the high efficiency of the particle activation in dry conditions (RH < 0.2 %) observed in our work. However, since O_3 and SO_2 can easily adsorb on the surface of the soot particles, some degree of competition cannot be ruled out. The second mechanism might dominate at low RH, while the first mechanism becomes competitive only at higher RH.

In conclusion, this study provides new insights on the role of each oxidation process leading to the transformation of soot into CCN. The analysis of the chemical composition of the aged soot particles shows that the variability of SO_4^{2-} and related ions found on the surface of soot particles is correlated to the increasing κ, which therefore become primary candidates to explain the CCN activation of chemically aged soot particles.

In Fig. 7, κ obtained for EXP4 is compared with our previous measurements carried out with kerosene soot exposed to O_3 and to OH radicals in a classic critical supersaturation (SS_c) against particle size (d_{ve} is used) diagram (Petters and Kreidenweis, 2007). All these experiments have been performed following the same experimental protocol. In particular, soot is sampled from the same kerosene flame at 130 mm HAB, size-selected at d_m = 150 nm (d_{ve} = 100 nm) using the same sampling system and aged in the same chamber. Fig. 7 provides a useful overview of κ, showing the wide range of values as a function of the chemical system used for the aging process.

To better estimate the atmospheric implications of our results, an equivalent atmospheric age is calculated for each experiment using typical tropospheric concentration ranges of the oxidizers. κ is shown in Table 2 with the corresponding atmospheric age that is found to be shorter than the typical lifetime of soot estimated from atmospheric modeling (Q. Wang et al., 2014; X. Wang et al., 2014). These new data are essential to understand the long- and short-term temporal variability in CCN measurements during field campaigns (Mei et al., 2021; Peng et al., 2020; Perkins et al., 2022; Schmale et al., 2018; Zheng et al., 2020). The CCN activation of soot by O_3 and SO_2 is a potentially competitive pathway for soot activation that should be taken into account in the modeling of the formation of clouds, as well as their lifetime and the evolution of their optical properties. Moreover, this work suggests that the activation of soot may occur directly on the particles in presence of both SO_2 and O_3.

More generally, SO_4^{2-} is a key anion in the atmosphere as it can participate to either homogenous or heterogeneous nucleation events. In the atmosphere, the rate of formation of SO_4^{2-} is driven by the oxidation of SO_2 by OH. In case of low OH concentration (during the night for instance) SO_2 can be oxidized by stabilized Criegee intermediate formed by the ozonolysis of unsaturated organics. Heterogeneous oxidation of SO_2 on the surface of particles (either solid or aqueous solutions) is also a pathway that complements the overview of the atmospheric SO_2 chemistry (Liu et al., 2021). Even if this gas phase chemistry is well-known, some model-measurements disagreement exist (Kasibhatla et al., 1997; Willis et al., 2018). In our opinion, this disagreement could be reduced if the contribution of multi-phase chemistry were adjusted in the chemical transport models for instance. Hence, there is the need for new laboratory measurements aiming to measure the kinetics constants that determine the SO_2/O_3 heterogeneous reactivity on carbonaceous particles, and on soot in particular.

In addition, it is reasonable to assume that the byproducts of the oxidation of the organics on the surface of the soot particles during SO_2/O_3 reactions gradually leads to the modification of the physicochemical properties of the surface, in particular their affinity for water and other polar species, which can lead to the formation of a coating that can ultimately affect the optical properties of the particles (Lefevre et al., 2019; Liu et al., 2016).

Concerning the hygroscopic parameter κ derived for each aerosol family, it seems necessary to extend this database by studying at laboratory scale under controlled and realistic atmospheric conditions the role of the complex mechanisms on the activation of soot, and in particular the effect of temperature and RH (Friebel and Mensah, 2019). This approach should also be applied to particles from other combustion processes (biomass burning or biofuels for instance). The results of these studies, coupled with field observations, should be used to feed global

climate models to provide better information on soot-cloud interactions and their adjustment effect on climate change.

CRediT authorship contribution statement

Junteng Wu: Investigation, Formal analysis, Writing – review & editing. **Alessandro Faccinetto:** Investigation, Formal analysis, Supervision, Writing – review & editing. **Sébastien Batut:** Investigation. **Mathieu Cazaunau:** Investigation. **Edouard Pangui:** Investigation. **Nicolas Nuns:** Investigation. **Benjamin Hanoune:** Funding acquisition, Writing – review & editing. **Jean-François Doussin:** Conceptualization, Writing – review & editing. **Pascale Desgroux:** Conceptualization, Investigation, Supervision, Writing – review & editing. **Denis Petitprez:** Conceptualization, Investigation, Supervision, Writing – original draft.

Declaration of competing interest

The authors declare that they have no known competing financial interests or personal relationships that could have appeared to influence the work reported in this paper.

Data availability

Data will be made available on request.

Acknowledgement

This work has received funding from the French national program LEFE/INSU (Les Enveloppes Fluides et l'Environnement/Institut National des Sciences de l'Univers) through the SulfuroSoot project. CNRS-INSU is gratefully acknowledged for supporting the CESAM chamber as a national facility as part of the French ACTRIS Research Infrastructure as well as the AERIS data center (www.aeris-data.fr) for distributing and curing the data produced by the CESAM chamber through the hosting of the EUROCHAMP datacenter (https://data.eurochamp.org). This work is a contribution to the LabEx CaPPA (Chemical and Physical Properties of the Atmosphere) project funded by the French National Research Agency (ANR) under contract "ANR-11-LABX-0005-01" and to the CPER research project CLIMIBIO funded by the French Ministère de l'Enseignement Supérieur et de la Recherche. The authors thank the Regional Council 'Hauts-de-France' and the European Regional Development Fund for their financial support for these projects. The Chevreul Institute is thanked for its help in the development of this work through the ARCHI-CM project supported by the "Ministère de l'Enseignement Supérieur de la Recherche et de l'Innovation", the region "Hauts-de-France", the ERDF program of the European Union and the "Métropole Européenne de Lille". The electron microscopy facility of the Chevreul Institute is also supported by the INSU.

References

Bellouin, N., Quaas, J., Gryspeerdt, E., Kinne, S., Stier, P., Watson-Parris, D., Boucher, O., Carslaw, K.S., Christensen, M., Daniau, A.-L., Dufresne, J.-L., Feingold, G., Fiedler, S., Forster, P., Gettelman, A., Haywood, J.M., Lohmann, U., Malavelle, F., Mauritsen, T., McCoy, D.T., Myhre, G., Mülmenstädt, J., Neubauer, D., Possner, A., Rugenstein, M., Sato, Y., Schulz, M., Schwartz, S.E., Sourdeval, O., Storelvmo, T., Toll, V., Winker, D., Stevens, B., 2020. Bounding global aerosol radiative forcing of climate change. Rev. Geophys. 58 https://doi.org/10.1029/2019RG000660 e2019RG000660.

Berndt, T., Jokinen, T., Mauldin, R.L.I., Petäjä, T., Herrmann, H., Junninen, H., Paasonen, P., Worsnop, D.R., Sipilä, M., 2012. Gas-phase ozonolysis of selected olefins: the yield of stabilized criegee intermediate and the reactivity toward SO2. J. Phys. Chem. Lett. 3, 2892–2896. https://doi.org/10.1021/jz301158u.

Bhandari, J., China, S., Chandrakar, K.K., Kinney, G., Cantrell, W., Shaw, R.A., Mazzoleni, L.R., Girotto, G., Sharma, N., Gorkowski, K., Gilardoni, S., Decesari, S., Facchini, M.C., Zanca, N., Pavese, G., Esposito, F., Dubey, M.K., Aiken, A.C., Chakrabarty, R.K., Moosmüller, H., Onasch, T.B., Zaveri, R.A., Scarnato, B.V., Fialho, P., Mazzoleni, C., 2019. Extensive soot compaction by cloud processing from laboratory and field observations. Sci. Rep. 9, 11824. https://doi.org/10.1038/s41598-019-48143-y.

Boichu, M., Favez, O., Riffault, V., Petit, J.-E., Zhang, Y., Brogniez, C., Sciare, J., Chiapello, I., Clarisse, L., Zhang, S., Pujol-Söhne, N., Tison, E., Delbarre, H., Goloub, P., 2019. Large-scale particulate air pollution and chemical fingerprint of volcanic sulfate aerosols from the 2014-2015 Holuhraun flood lava eruption of Bárðarbunga volcano (Iceland). Atmos. Chem. Phys. 19, 14253–14287. https://doi.org/10.5194/acp-19-14253-2019.

Bond, T.C., Bergstrom, R.W., 2006. Light absorption by carbonaceous particles: an investigative review. Aerosol Sci. Technol. 40, 27–67. https://doi.org/10.1080/02786820500421521.

Cheng, Y., Zheng, G., Wei, C., Mu, Q., Zheng, B., Wang, Z., Gao, M., Zhang, Q., He, K., Carmichael, G., Pöschl, U., Su, H., 2016. Reactive nitrogen chemistry in aerosol water as a source of sulfate during haze events in China. Sci. Adv. 2, e1601530 https://doi.org/10.1126/sciadv.1601530.

Chughtai, A.R., Atteya, M.M.O., Kim, J., Konowalchuk, B.K., Smith, D.M., 1998. Adsorption and adsorbate interaction at soot particle surfaces. Carbon 36, 1573–1589. https://doi.org/10.1016/S0008-6223(98)00116-X.

D'Anna, A., 2009. Combustion-formed nanoparticles. Proc. Combust. Inst. 32, 593–613. https://doi.org/10.1016/j.proci.2008.09.005.

Denjean, C., Formenti, P., Picquet-Varrault, B., Camredon, M., Pangui, E., Zapf, P., Katrib, Y., Giorio, C., Tapparo, A., Temime-Roussel, B., Monod, A., Aumont, B., Doussin, J.F., 2015. Aging of secondary organic aerosol generated from the ozonolysis of α-pinene: effects of ozone, light and temperature. Atmos. Chem. Phys. 15, 883–897. https://doi.org/10.5194/acp-15-883-2015.

Doussin, J.-F., Fuchs, H., Kiendler-Scharr, A., Seakins, P., Wenger, J., 2023. A Practical Guide to Atmospheric Simulation Chambers, 1st ed. Springer Cham.

Faccinetto, A., Irimiea, C., Minutolo, P., Commodo, M., D'Anna, A., Nuns, N., Carpentier, Y., Pirim, C., Desgroux, P., Focsa, C., Mercier, X., 2020. Evidence on the formation of dimers of polycyclic aromatic hydrocarbons in a laminar diffusion flame. Commun. Chem. 3, 112. https://doi.org/10.1038/s42004-020-00357-2.

Friebel, F., Mensah, A.A., 2019. Ozone concentration versus temperature: atmospheric aging of soot particles. Langmuir 35, 14437–14450. https://doi.org/10.1021/acs.langmuir.9b02372.

Friebel, F., Lobo, P., Neubauer, D., Lohmann, U., Drossaart van Dusseldorp, S., Mühlhofer, E., Mensah, A.A., 2019. Impact of isolated atmospheric aging processes on the cloud condensation nuclei activation of soot particles. Atmos. Chem. Phys. 19, 15545–15567. https://doi.org/10.5194/acp-19-15545-2019.

Grimonprez, S., Faccinetto, A., Batut, S., Wu, J., Desgroux, P., Petitprez, D., 2018. Cloud condensation nuclei from the activation with ozone of soot particles sampled from a kerosene diffusion flame. Aerosol Sci. Technol. 52, 814–827. https://doi.org/10.1080/02786826.2018.1472367.

Grimonprez, S., Wu, J., Faccinetto, A., Gosselin, S., Riber, E., Cuenot, B., Cazaunau, M., Pangui, E., Formenti, P., Doussin, J.-F., Petitprez, D., Desgroux, P., 2021. Hydrophilic properties of soot particles exposed to OH radicals: a possible new mechanism involved in the contrail formation. Proc. Combust. Inst. 38, 6441–6450. https://doi.org/10.1016/j.proci.2020.06.306.

Gross, S., Bertram, A.K., 2008. Reactive uptake of NO3, N2O5, NO2, HNO3, and O3 on three types of polycyclic aromatic hydrocarbon surfaces. J. Phys. Chem. A 112, 3104–3113. https://doi.org/10.1021/jp7107544.

Guilloteau, A., Bedjanian, Y., Nguyen, M.L., Tomas, A., 2010. Desorption of polycyclic aromatic hydrocarbons from a soot surface: three- to five-ring PAHs. J. Phys. Chem. A 114, 942–948. https://doi.org/10.1021/jp908862c.

Hagen, D.E., Trueblood, M.B., White, D.R., 1989. Hydration properties of combustion aerosols. Aerosol Sci. Technol. 10, 63–69. https://doi.org/10.1080/02786828908959221.

Han, C., Liu, Y., Ma, J., He, H., 2012. Key role of organic carbon in the sunlight-enhanced atmospheric aging of soot by O2. Proc. Natl. Acad. Sci. 109, 21250–21255. https://doi.org/10.1073/pnas.1212690110.

Hansen, J., Nazarenko, L., 2004. Soot climate forcing via snow and ice albedos. Proc. Natl. Acad. Sci. 101, 423–428. https://doi.org/10.1073/pnas.2237157100.

He, C., Li, Q., Liou, K.-N., Qi, L., Tao, S., Schwarz, J.P., 2016. Microphysics-based black carbon aging in a global CTM: constraints from HIPPO observations and implications for global black carbon budget. Atmos. Chem. Phys. 16, 3077–3098. https://doi.org/10.5194/acp-16-3077-2016.

He, G., He, H., 2020. Water promotes the oxidation of SO2 by O2 over carbonaceous aerosols. Environ. Sci. Technol. 54, 7070–7077. https://doi.org/10.1021/acs.est.0c00021.

He, G., Ma, J., He, H., 2018. Role of carbonaceous aerosols in catalyzing sulfate formation. ACS Catal. 8, 3825–3832. https://doi.org/10.1021/acscatal.7b04195.

He, X., Pang, S., Ma, J., Zhang, Y., 2017. Influence of relative humidity on heterogeneous reactions of O3 and O3/SO2 with soot particles: potential for environmental and health effects. Atmos. Environ. 165, 198–206. https://doi.org/10.1016/j.atmosenv.2017.06.049.

Irimiea, C., Faccinetto, A., Carpentier, Y., Ortega, I.-K., Nuns, N., Therssen, E., Desgroux, P., Focsa, C., 2018. A comprehensive protocol for chemical analysis of flame combustion emissions by secondary ion mass spectrometry. Rapid Commun. Mass Spectrom. 32, 1015–1025. https://doi.org/10.1002/rcm.8133.

Irimiea, C., Faccinetto, A., Mercier, X., Ortega, I.-K., Nuns, N., Therssen, E., Desgroux, P., Focsa, C., 2019. Unveiling trends in soot nucleation and growth: when secondary ion mass spectrometry meets statistical analysis. Carbon 144, 815–830. https://doi.org/10.1016/j.carbon.2018.12.015.

Kärcher, B., 2018. Formation and radiative forcing of contrail cirrus. Nat. Commun. 9, 1824. https://doi.org/10.1038/s41467-018-04068-0.

Kasibhatla, P., Chameides, W.L., John, J.St., 1997. A three-dimensional global model investigation of seasonal variations in the atmospheric burden of anthropogenic sulfate aerosols. J. Geophys. Res. Atmos. 102, 3737–3759. https://doi.org/10.1029/96JD03084.

Khou, J.C., Ghedhaïfi, W., Vancassel, X., Montreuil, E., Garnier, F., 2017. CFD simulation of contrail formation in the near field of a commercial aircraft: effect of fuel sulfur content. Meteorol. Z. 26, 585–596. https://doi.org/10.1127/metz/2016/0761.

Kirkby, J., Curtius, J., Almeida, J., Dunne, E., Duplissy, J., Ehrhart, S., Franchin, A., Gagné, S., Ickes, L., Kürten, A., Kupc, A., Metzger, A., Riccobono, F., Rondo, L., Schobesberger, S., Tsagkogeorgas, G., Wimmer, D., Amorim, A., Bianchi, F., Breitenlechner, M., David, A., Dommen, J., Downard, A., Ehn, M., Flagan, R.C., Haider, S., Hansel, A., Hauser, D., Jud, W., Junninen, H., Kreissl, F., Kvashin, A., Laaksonen, A., Lehtipalo, K., Lima, J., Lovejoy, E.R., Makhmutov, V., Mathot, S., Mikkilä, J., Minginette, P., Mogo, S., Nieminen, T., Onnela, A., Pereira, P., Petäjä, T., Schnitzhofer, R., Seinfeld, J.H., Sipilä, M., Stozhkov, Y., Stratmann, F., Tomé, A., Vanhanen, J., Viisanen, Y., Vrtala, A., Wagner, P.E., Walther, H., Weingartner, E., Wex, H., Winkler, P.M., Carslaw, K.S., Worsnop, D.R., Baltensperger, U., Kulmala, M., 2011. Role of sulphuric acid, ammonia and galactic cosmic rays in atmospheric aerosol nucleation. Nature 476, 429–433. https://doi.org/10.1038/nature10343.

Klöwer, M., Allen, M.R., Lee, D.S., Proud, S.R., Gallagher, L., Skowron, A., 2021. Quantifying aviation's contribution to global warming. Environ. Res. Lett. 16, 104027 https://doi.org/10.1088/1748-9326/ac286e.

Kourtchev, I., Doussin, J.-F., Giorio, C., Mahon, B., Wilson, E.M., Maurin, N., Pangui, E., Venables, D.S., Wenger, J.C., Kalberer, M., 2015. Molecular composition of fresh and aged secondary organic aerosol from a mixture of biogenic volatile compounds: a high-resolution mass spectrometry study. Atmos. Chem. Phys. 15, 5683–5695. https://doi.org/10.5194/acp-15-5683-2015.

Lambe, A.T., Ahern, A.T., Wright, J.P., Croasdale, D.R., Davidovits, P., Onasch, T.B., 2015. Oxidative aging and cloud condensation nuclei activation of laboratory combustion soot. J. Aerosol Sci. 79, 31–39. https://doi.org/10.1016/j.jaerosci.2014.10.001.

Lefevre, G., Yon, J., Bouvier, M., Liu, F., Coppalle, A., 2019. Impact of organic coating on soot angular and spectral scattering properties. Environ. Sci. Technol. 53, 6383–6391. https://doi.org/10.1021/acs.est.8b05482.

Lelievre, S., Bedjanian, Y., Pouvesle, N., Delfau, J.-L., Vovelle, C., Le Bras, G., 2004. Heterogeneous reaction of ozone with hydrocarbon flame soot. Phys. Chem. Chem. Phys. 6, 1181–1191. https://doi.org/10.1039/B316895F.

Lemaire, R., Faccinetto, A., Therssen, E., Ziskind, M., Focsa, C., Desgroux, P., 2009. Experimental comparison of soot formation in turbulent flames of diesel and surrogate diesel fuels. Proc. Combust. Inst. 32, 737–744. https://doi.org/10.1016/j.proci.2008.05.019.

Lemaire, R., Therssen, E., Desgroux, P., 2010. Effect of ethanol addition in gasoline and gasoline–surrogate on soot formation in turbulent spray flames. Fuel 89, 3952–3959. https://doi.org/10.1016/j.fuel.2010.06.031.

Li, K., Chen, L., Han, K., Lv, B., Bao, K., Wu, X., Gao, X., Cen, K., 2017. Smog chamber study on aging of combustion soot in isoprene/SO2/NOx system: changes of mass, size, effective density, morphology and mixing state. Atmos. Res. 184, 139–148. https://doi.org/10.1016/j.atmosres.2016.10.011.

Li, L., Chen, Z.M., Zhang, Y.H., Zhu, T., Li, J.L., Ding, J., 2006. Kinetics and mechanism of heterogeneous oxidation of sulfur dioxide by ozone on surface of calcium carbonate. Atmos. Chem. Phys. 6, 2453–2464. https://doi.org/10.5194/acp-6-2453-2006.

Li, M., Bao, F., Zhang, Y., Song, W., Chen, C., Zhao, J., 2018. Role of elemental carbon in the photochemical aging of soot. Proc. Natl. Acad. Sci. 115, 7717–7722. https://doi.org/10.1073/pnas.1804481115.

Li, M., Li, J., Zhu, Y., Chen, J., Andreae, M.O., Pöschl, U., Su, H., Kulmala, M., Chen, C., Cheng, Y., Zhao, J., 2022. Highly oxygenated organic molecules with high unsaturation formed upon photochemical aging of soot. Chem 8, 2688–2699. https://doi.org/10.1016/j.chempr.2022.06.011.

Liu, F., Yon, J., Bescond, A., 2016. On the radiative properties of soot aggregates - part 2: effects of coating. J. Quant. Spectrosc. Radiat. Transf. 172, 134–145. https://doi.org/10.1016/j.jqsrt.2015.08.005.

Liu, T., Chan, A.W.H., Abbatt, J.P.D., 2021. Multiphase oxidation of sulfur dioxide in aerosol particles: implications for sulfate formation in polluted environments. Environ. Sci. Technol. 55, 4227–4242. https://doi.org/10.1021/acs.est.0c06496.

Liu, Y., Liu, C., Ma, J., Ma, Q., He, H., 2010. Structural and hygroscopic changes of soot during heterogeneous reaction with O3. Phys. Chem. Chem. Phys. 12, 10896–10903. https://doi.org/10.1039/C0CP00402B.

Liu, Y., He, G., Chu, B., Ma, Q., He, H., 2022. Atmospheric heterogeneous reactions on soot: a review. Fundam. Res. https://doi.org/10.1016/j.fmre.2022.02.012.

Lohmann, U., Friebel, F., Kanji, Z.A., Mahrt, F., Mensah, A.A., Neubauer, D., 2020. Future warming exacerbated by aged-soot effect on cloud formation. Nat. Geosci. 13, 674–680. https://doi.org/10.1038/s41561-020-0631-0.

Ma, Q., Zhang, C., Liu, C., He, G., Zhang, P., Li, H., Chu, B., He, H., 2023. A review on the heterogeneous oxidation of SO2 on solid atmospheric particles: implications for sulfate formation in haze chemistry. Crit. Rev. Environ. Sci. Technol. 53, 1888–1911. https://doi.org/10.6084/m9.figshare.22456382.v1.

Mahrt, F., Marcolli, C., David, R.O., Grönquist, P., Barthazy Meier, E.J., Lohmann, U., Kanji, Z.A., 2018. Ice nucleation abilities of soot particles determined with the Horizontal Ice Nucleation Chamber. Atmos. Chem. Phys. 18, 13363–13392. https://doi.org/10.5194/acp-18-13363-2018.

Mallet, M., Solmon, F., Nabat, P., Elguindi, N., Waquet, F., Bouniol, D., Sayer, A.M., Meyer, K., Roehrig, R., Michou, M., Zuidema, P., Flamant, C., Redemann, J., Formenti, P., 2020. Direct and semi-direct radiative forcing of biomass-burning aerosols over the southeast Atlantic (SEA) and its sensitivity to absorbing properties: a regional climate modeling study. Atmos. Chem. Phys. 20, 13191–13216. https://doi.org/10.5194/acp-20-13191-2020.

Mao, J., Ren, X., Brune, W.H., Olson, J.R., Crawford, J.H., Fried, A., Huey, L.G., Cohen, R.C., Heikes, B., Singh, H.B., Blake, D.R., Sachse, G.W., Diskin, G.S., Hall, S. R., Shetter, R.E., 2009. Airborne measurement of OH reactivity during INTEX-B. Atmos. Chem. Phys. 9, 163–173. https://doi.org/10.5194/acp-9-163-2009.

Martin, J.W., Salamanca, M., Kraft, M., 2022. Soot inception: carbonaceous nanoparticle formation in flames. Prog. Energy Combust. Sci. 88, 100956 https://doi.org/10.1016/j.pecs.2021.100956.

Mei, F., Wang, J., Zhou, S., Zhang, Q., Collier, S., Xu, J., 2021. Measurement report: cloud condensation nuclei activity and its variation with organic oxidation level and volatility observed during an aerosol life cycle intensive operational period (ALC-IOP). Atmos. Chem. Phys. 21, 13019–13029. https://doi.org/10.5194/acp-21-13019-2021.

Moteki, N., 2023. Climate-relevant properties of black carbon aerosols revealed by in situ measurements: a review. Prog. Earth Planet. Sci. 10, 12. https://doi.org/10.1186/s40645-023-00544-4.

Novakov, T., Chang, S.G., Harker, A.B., 1974. Sulfates as pollution particulates: catalytic formation on carbon (soot) particles. Science 186, 259–261.

Parrish, D.D., Derwent, R.G., Staehelin, J., 2021. Long-term changes in northern mid-latitude tropospheric ozone concentrations: synthesis of two recent analyses. Atmos. Environ. 248, 118227 https://doi.org/10.1016/j.atmosenv.2021.118227.

Peng, C., Wang, Y., Wu, Z., Chen, L., Huang, R.-J., Wang, W., Wang, Z., Hu, W., Zhang, G., Ge, M., Hu, M., Wang, X., Tang, M., 2020. Tropospheric aerosol hygroscopicity in China. Atmos. Chem. Phys. 20, 13877–13903. https://doi.org/10.5194/acp-20-13877-2020.

Peng, J., Hu, M., Guo, S., Du, Z., Zheng, Jing, Shang, D., Levy Zamora, M., Zeng, L., Shao, M., Wu, Y.-S., Zheng, Jun, Wang, Y., Glen, C.R., Collins, D.R., Molina, M.J., Zhang, R., 2016. Markedly enhanced absorption and direct radiative forcing of black carbon under polluted urban environments. Proc. Natl. Acad. Sci. 113, 4266–4271. https://doi.org/10.1073/pnas.1602310113.

Peng, J., Hu, M., Guo, S., Du, Z., Zheng, Jing, Zheng, Jun, Zeng, L., Shao, M., Wu, Y., Collins, D., Zhang, R., 2017. Ageing and hygroscopicity variation of black carbon particles in Beijing measured by a quasi-atmospheric aerosol evolution study (QUALITY) chamber. Atmos. Chem. Phys. 17, 10333–10348. https://doi.org/10.5194/acp-17-10333-2017.

Perkins, R.J., Marinescu, P.J., Levin, E.J.T., Collins, D.R., Kreidenweis, S.M., 2022. Long- and short-term temporal variability in cloud condensation nuclei spectra over a wide supersaturation range in the Southern Great Plains site. Atmos. Chem. Phys. 22, 6197–6215. https://doi.org/10.5194/acp-22-6197-2022.

Petters, M.D., Kreidenweis, S.M., 2007. A single parameter representation of hygroscopic growth and cloud condensation nucleus activity. Atmos. Chem. Phys. 7, 1961–1971. https://doi.org/10.5194/acp-7-1961-2007.

Petzold, A., Gysel, M., Vancassel, X., Hitzenberger, R., Puxbaum, H., Vrochticky, S., Weingartner, E., Baltensperger, U., Mirabel, P., 2005. On the effects of organic matter and sulphur-containing compounds on the CCN activation of combustion particles. Atmos. Chem. Phys. 5, 3187–3203. https://doi.org/10.5194/acp-5-3187-2005.

Popovicheva, O.B., Persiantseva, N.M., Tishkova, V., Shonija, N.K., Zubareva, N.A., 2008. Quantification of water uptake by soot particles. Environ. Res. Lett. 3, 025009 https://doi.org/10.1088/1748-9326/3/2/025009.

Quan, J., Liu, Q., Li, X., Gao, Y., Jia, X., Sheng, J., Liu, Y., 2015. Effect of heterogeneous aqueous reactions on the secondary formation of inorganic aerosols during haze events. Atmos. Environ. 122, 306–312. https://doi.org/10.1016/j.atmosenv.2015.09.068.

Riccobono, F., Schobesberger, S., Scott, C.E., Dommen, J., Ortega, I.K., Rondo, L., Almeida, J., Amorim, A., Bianchi, F., Breitenlechner, M., David, A., Downard, A., Dunne, E.M., Duplissy, J., Ehrhart, S., Flagan, R.C., Franchin, A., Hansel, A., Junninen, H., Kajos, M., Keskinen, H., Kupc, A., Kürten, A., Kvashin, A.N., Laaksonen, A., Lehtipalo, K., Makhmutov, V., Mathot, S., Nieminen, T., Onnela, A., Petäjä, T., Praplan, A.P., Santos, F.D., Schallhart, S., Seinfeld, J.H., Sipilä, M., Spracklen, D.V., Stozhkov, Y., Stratmann, F., Tomé, A., Tsagkogeorgas, G., Vaattovaara, P., Viisanen, Y., Vrtala, A., Wagner, P.E., Weingartner, E., Wex, H., Wimmer, D., Carslaw, K.S., Curtius, J., Donahue, N.M., Kirkby, J., Kulmala, M., Worsnop, D.R., Baltensperger, U., 2014. Oxidation products of biogenic emissions contribute to nucleation of atmospheric particles. Science 344, 717–721. https://doi.org/10.1126/science.1243527.

Schmale, J., Henning, S., Decesari, S., Henzing, B., Keskinen, H., Sellegri, K., Ovadnevaite, J., Pöhlker, M.L., Brito, J., Bougiatioti, A., Kristensson, A., Kalivitis, N., Stavroulas, I., Carbone, S., Jefferson, A., Park, M., Schlag, P., Iwamoto, Y., Aalto, P., Äijälä, M., Bukowiecki, N., Ehn, M., Frank, G., Fröhlich, R., Frumau, A., Herrmann, E., Herrmann, H., Holzinger, R., Kos, G., Kulmala, M., Mihalopoulos, N., Nenes, A., O'Dowd, C., Petäjä, T., Picard, D., Pöhlker, C., Pöschl, U., Poulain, L., Prévôt, A.S.H., Swietlicki, E., Andreae, M.O., Artaxo, P., Wiedensohler, A., Ogren, J., Matsuki, A., Yum, S.S., Stratmann, F., Baltensperger, U., Gysel, M., 2018. Long-term cloud condensation nuclei number concentration, particle number size distribution and chemical composition measurements at regionally representative observatories. Atmos. Chem. Phys. 18, 2853–2881. https://doi.org/10.5194/acp-18-2853-2018.

Schumann, U., Baumann, R., Baumgardner, D., Bedka, S.T., Duda, D.P., Freudenthaler, V., Gayet, J.-F., Heymsfield, A.J., Minnis, P., Quante, M., Raschke, E., Schlager, H., Vázquez-Navarro, M., Voigt, C., Wang, Z., 2017. Properties of individual contrails: a compilation of observations and some comparisons. Atmos. Chem. Phys. 17, 403–438. https://doi.org/10.5194/acp-17-403-2017.

Sipilä, M., Berndt, T., Petäjä, T., Brus, D., Vanhanen, K., Stratmann, F., Patokoski, J., Mauldin, R.L., Hyvärinen, A.-P., Lihavainen, H., Kulmala, M., 2010. The role of sulfuric acid in atmospheric nucleation. Science 327, 1243–1246. https://doi.org/10.1126/science.1180315.

Smooke, M.D., Long, M.B., Connelly, B.C., Colket, M.B., Hall, R.J., 2005. Soot formation in laminar diffusion flames. Combust. Flame 143, 613–628. https://doi.org/10.1016/j.combustflame.2005.08.028.

Stockwell, W.R., Calvert, J.G., 1983. The mechanism of the HO-SO2 reaction. Atmos. Environ. 17, 2231–2235. https://doi.org/10.1016/0004-6981(83)90220-2.

Stone, D., Whalley, L.K., Heard, D.E., 2012. Tropospheric OH and HO2 radicals: field measurements and model comparisons. Chem. Soc. Rev. 41, 6348–6404. https://doi.org/10.1039/C2CS35140D.

Su, H., Rose, D., Cheng, Y.F., Gunthe, S.S., Massling, A., Stock, M., Wiedensohler, A., Andreae, M.O., Pöschl, U., 2010. Hygroscopicity distribution concept for measurement data analysis and modeling of aerosol particle mixing state with regard to hygroscopic growth and CCN activation. Atmos. Chem. Phys. 10, 7489–7503. https://doi.org/10.5194/acp-10-7489-2010.

Szopa, S., Naik, V., Adhikary, B., Artaxo, P., Berntsen, T., Collins, W.D., Fuzzi, S., Gallardo, L., Kiendler-Scharr, A., Klimont, Z., Liao, H., Unger, N., Zanis, P., 2021. Short-lived climate forcers. In: Climate Change 2021: The Physical Science Basis. Contribution of Working Group I to the Sixth Assessment Report of the Intergovernmental Panel on Climate Change. Cambridge University Press, Cambridge, United Kingdom and New York, NY, US, pp. 817–922.

Tritscher, T., Jurányi, Z., Martin, M., Chirico, R., Gysel, M., Heringa, M.F., DeCarlo, P.F., Sierau, B., Prévôt, A.S.H., Weingartner, E., Baltensperger, U., 2011. Changes of hygroscopicity and morphology during ageing of diesel soot. Environ. Res. Lett. 6, 034026 https://doi.org/10.1088/1748-9326/6/3/034026.

Wang, H., 2011. Formation of nascent soot and other condensed-phase materials in flames. Proc. Combust. Inst. 33, 41–67. https://doi.org/10.1016/j.proci.2010.09.009.

Wang, J., Doussin, J.F., Perrier, S., Perraudin, E., Katrib, Y., Pangui, E., Picquet-Varrault, B., 2011. Design of a new multi-phase experimental simulation chamber for atmospheric photosmog, aerosol and cloud chemistry research. Atmos. Meas. Tech. 4, 2465–2494. https://doi.org/10.5194/amt-4-2465-2011.

Wang, Q., Jacob, D.J., Spackman, J.R., Perring, A.E., Schwarz, J.P., Moteki, N., Marais, E. A., Ge, C., Wang, J., Barrett, S.R.H., 2014b. Global budget and radiative forcing of black carbon aerosol: constraints from pole-to-pole (HIPPO) observations across the Pacific. J. Geophys. Res. Atmos. 119, 195–206. https://doi.org/10.1002/2013JD020824.

Wang, X., Heald, C.L., Ridley, D.A., Schwarz, J.P., Spackman, J.R., Perring, A.E., Coe, H., Liu, D., Clarke, A.D., 2014a. Exploiting simultaneous observational constraints on mass and absorption to estimate the global direct radiative forcing of black carbon and brown carbon. Atmos. Chem. Phys. 14, 10989–11010. https://doi.org/10.5194/acp-14-10989-2014.

Weingartner, E., Burtscher, H., Baltensperger, U., 1997. Hygroscopic properties of carbon and diesel soot particles. Atmos. Environ. 31, 2311–2327. https://doi.org/10.1016/S1352-2310(97)00023-X.

Willis, M..D., Leaitch, W.R., Abbatt, J.P.D., 2018. Processes controlling the composition and abundance of arctic aerosol. Rev. Geophys. 56, 621–671. https://doi.org/10.1029/2018RG000602.

Wittbom, C., Eriksson, A.C., Rissler, J., Carlsson, J.E., Roldin, P., Nordin, E.Z., Nilsson, P. T., Swietlicki, E., Pagels, J.H., Svenningsson, B., 2014. Cloud droplet activity changes of soot aerosol upon smog chamber ageing. Atmos. Chem. Phys. 14, 9831–9854. https://doi.org/10.5194/acp-14-9831-2014.

Wu, J., Faccinetto, A., Grimonprez, S., Batut, S., Yon, J., Desgroux, P., Petitprez, D., 2020. Influence of the dry aerosol particle size distribution and morphology on the cloud condensation nuclei activation. An experimental and theoretical investigation. Atmos. Chem. Phys. 20, 4209–4225. https://doi.org/10.5194/acp-20-4209-2020.

Xu, W., Li, Q., Shang, J., Liu, J., Feng, X., Zhu, T., 2015. Heterogeneous oxidation of SO2 by O3-aged black carbon and its dithiothreitol oxidative potential. J. Environ. Sci. 36, 56–62. https://doi.org/10.1016/j.jes.2015.02.014.

Yasmeen, F., Vermeylen, R., Maurin, N., Perraudin, E., Doussin, J.-F., Claeys, M., 2012. Characterisation of tracers for aging of α-pinene secondary organic aerosol using liquid chromatography/negative ion electrospray ionisation mass spectrometry. Environ. Chem. 9, 236–246. https://doi.org/10.1071/EN11148.

Yon, J., Bescond, A., Ouf, F.-X., 2015. A simple semi-empirical model for effective density measurements of fractal aggregates. J. Aerosol Sci. 87, 28–37. https://doi.org/10.1016/j.jaerosci.2015.05.003.

Zhang, R., Khalizov, A.F., Pagels, J., Zhang, D., Xue, H., McMurry, P.H., 2008. Variability in morphology, hygroscopicity, and optical properties of soot aerosols during atmospheric processing. Proc. Natl. Acad. Sci. 105, 10291–10296. https://doi.org/10.1073/pnas.0804860105.

Zhao, D.F., Buchholz, A., Kortner, B., Schlag, P., Rubach, F., Kiendler-Scharr, A., Tillmann, R., Wahner, A., Flores, J.M., Rudich, Y., Watne, Å.K., Hallquist, M., Wildt, J., Mentel, T.F., 2015. Size-dependent hygroscopicity parameter (κ) and chemical composition of secondary organic cloud condensation nuclei. Geophys. Res. Lett. 42, 10,920–10,928. https://doi.org/10.1002/2015GL066497.

Zhao, Y., Liu, Y., Ma, J., Ma, Q., He, H., 2017. Heterogeneous reaction of SO2 with soot: the roles of relative humidity and surface composition of soot in surface sulfate formation. Atmos. Environ. 152, 465–476. https://doi.org/10.1016/j.atmosenv.2017.01.005.

Zheng, G., Kuang, C., Uin, J., Watson, T., Wang, J., 2020. Large contribution of organics to condensational growth and formation of cloud condensation nuclei (CCN) in the remote marine boundary layer. Atmos. Chem. Phys. 20, 12515–12525. https://doi.org/10.5194/acp-20-12515-2020.